Supplement of Hydrol. Earth Syst. Sci., 30, 2183–2206, 2026
https://doi.org/10.5194/hess-30-2183-2026-supplement

Hydrology and Earth System Sciences
Open Access
EGU

Supplement of

Community-scale urban flood monitoring through fusion of time-lapse imagery, terrestrial lidar, and remote sensing data

Jedidiah E. Dale et al.

Correspondence to: Jedidiah E. Dale (jed@wustl.edu)

S1: HEC-RAS Rain-on-Grid (ROG) model development

Model domain: The computational mesh was generated from a TIN-interpolated gap filled, 0.5 m resolution DTM generated from 2019 USGS 3DEP aerial lidar data. The base mesh was generated with 10 m node spacing. Breaklines were added for channel centerlines, culvert inflows and storm drains. Mesh refinement was applied within 5 m of these breaklines, reducing node spacing to 1 m for the area of interest.

1D-2D Connections: 1D connections were added for known culverts at road crossings. Individual measurements were unavailable, and a diameter of 1m, Mannings'*n* of 0.015 and weir coefficients of 0.5 were used for all culverts.

Stormwater system: The combined sewer-stormwater system was modeled as a 1D pipe network in HEC-RAS. The location of stormwater inflows was taken from the Illinois Department of Natural Resources (IDNR) and Heartlands Institute survey of the Prairie Du Pont Watershed. Precise information on the topology and hydraulics of the sewer-stormwater system is unavailable, and connections between inflows was inferred based on published IDNR and USACE reports and maps (USACE 2024; IDNR 2023). Pipe diameter of 0.7 m, based on IDNR survey, and n of 0.015 m were used, based on USACE reported values. The pipe network was connected to the know drainage ditch outfall.

Mannings roughness (n): 30 m resolution data from the National Land Cover Database (NLCD) were used to define spatially variable roughness coefficients, using HEC-RAS manual reference values for each classification. This was refined using vector polygons of road surfaces and building footprints from the Illinois Department of Transportation and Illinois Water Survey. Within building footprints *n* was assigned a high value of 10 which prevents the routing of runoff from those cells.

Rainfall Runoff: The curve number (CN) method was used to calculate initial infiltration losses and runoff generation. The same NLCD landcover, and IDOT building and road layers were used to define spatially variable values for CN, abstraction ratio and minimum infiltration rate. Reference values were taken from the HEC-RAS hydraulics manual, with abstraction ratios suggested by Hawkins and Jiang 2023. No additional infiltration losses are calculated after the initial rainfall-runoff conversion.

Boundary conditions: A 2D flow area was defined over the study area with a total area of 89.6 km2. A normal depth boundary condition was defined at the border of the model domain with the large drainage ditch bounding the model domain. The 30 min interval precipitation record from either KCPS (15 May) or ENGM7 (4 July), was used to define an unsteady precipitation hydrograph boundary condition. Spatial variability in precipitation was not included.

Simulation parameters: Models were run with a 10 second computational interval, with a 5 min interval for data export. Model runs were performed in HEC-RAS version 6.60 on a 32 core AMD Ryzen 3970X with 128GB of RAM.

Land Cover Classification	Manning's N Value
NoData	0.035
Roads	0.01
Buildings	10
Banks	0.04
MainChannel	0.03
Open Water	0.035
Developed, Open Space	0.035
Developed, Low Intensity	0.08
Developed, Medium Intensity	0.12
Developed, High Intensity	0.15
Barren Land Rock/Sand/Clay	0.025
Deciduous Forest	0.15
Evergreen Forest	0.15
Mixed Forest	0.1
Shrub/Scrub	0.9
Grassland/Herbaceous	0.04
Pasture/Hay	0.045
Cultivated Crops	0.05
Woody Wetlands	0.07
Emergent Herbaceous Wetlands	0.07

Table S1: Reference landcover based Manning 's roughness coefficients taken from USACE 2024.

Name (Land Cover: Soil Hydric Group)	**Curve Number**	**Initial Abstraction Ratio**	**Abstraction Ratio**	**Minimum Infiltration Rate**
Developed, Medium Intensity : D	86	0.05	0.082	1.270
Developed, Open Space : B/D	74	0.05	0.176	3.485
Emergent Herbaceous Wetlands : A	76	0.05	0.158	7.600
Grassland/Herbaceous : D	80	0.05	0.125	1.270
Buildings :	100	0.05	0.000	0.000
Roads : C	98	0.05	0.010	0.000

Table S2: Reference runoff parameters taken from USACE 2024 & Hawkins & Jiang 2023

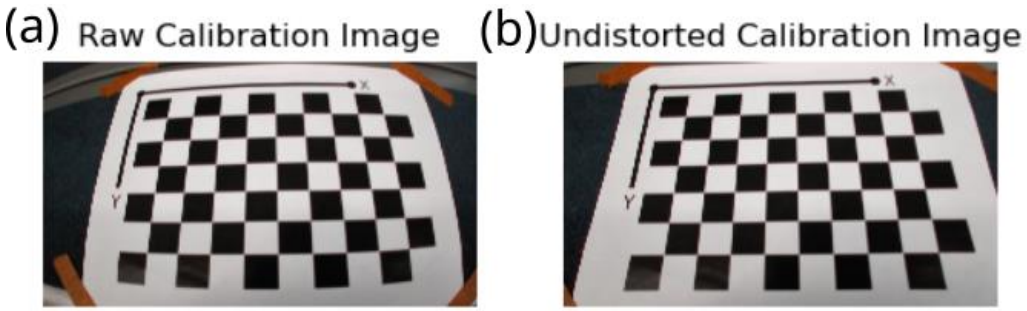

Figure S1: Example of a calibration image (a) before and (b) after correction with estimated distortion coefficients.

Distortion corrected projection

Wide field-of-view (FOV) cameras with a short focal length, such as many trail and security cameras, can be particularly susceptible to distortion, making it important to account for during both camera pose estimation, and 3D to 2D point projection. A set of five coefficients describing radial distortion (k_1, k_2, k_3) and tangential distortion (p_1, p_2) are estimated during camera calibration and summarized by the distortion vector, d.

$$d = [k_1 \quad k_2 \quad p_1 \quad p_2 \quad k_3]. \tag{S1}$$

Distortion coefficients are applied after transformation with the extrinsic matrix, **P,** and before projection with the intrinsic matrix **K.** For additional details on implementation see the OpenCV documentation at: https://docs.opencv.org/4.x/d9/d0c/group__calib3d.html (Bradski, 2000).

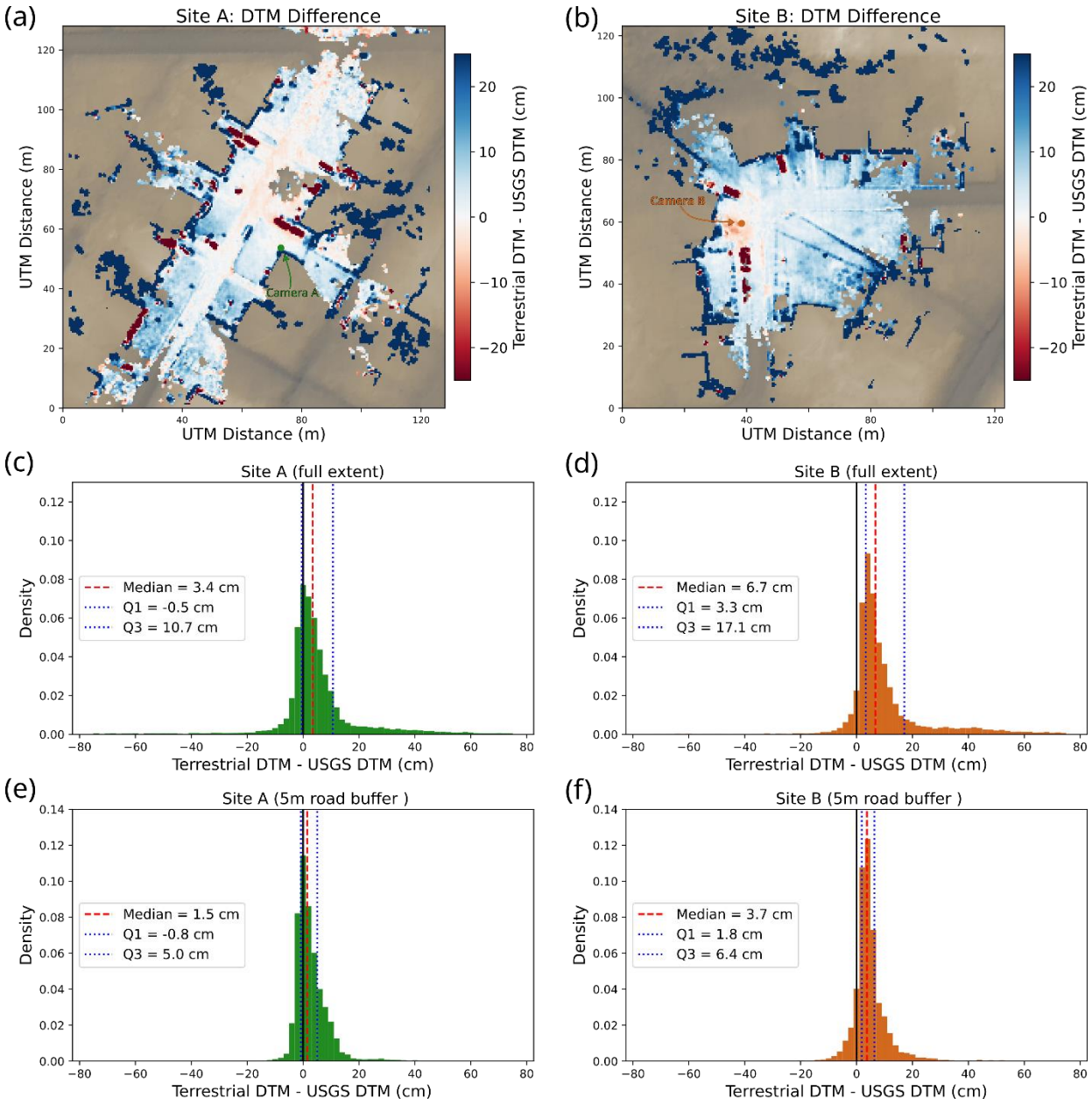

Figure S2: Elevation differences between the 0.5 m-resolution, georeferenced terrestrial lidar DTM (2023), and 0.5 m-resolution aerial USGS lidar DTM (2020) at (a) Site A and (a) Site B. Larger elevation differences are found around the edge of the survey extent, and where vehicles were present during the aerial scan (visible as red patches). However, differences are generally below 5 cm within 5 m of the road surface (c-f).

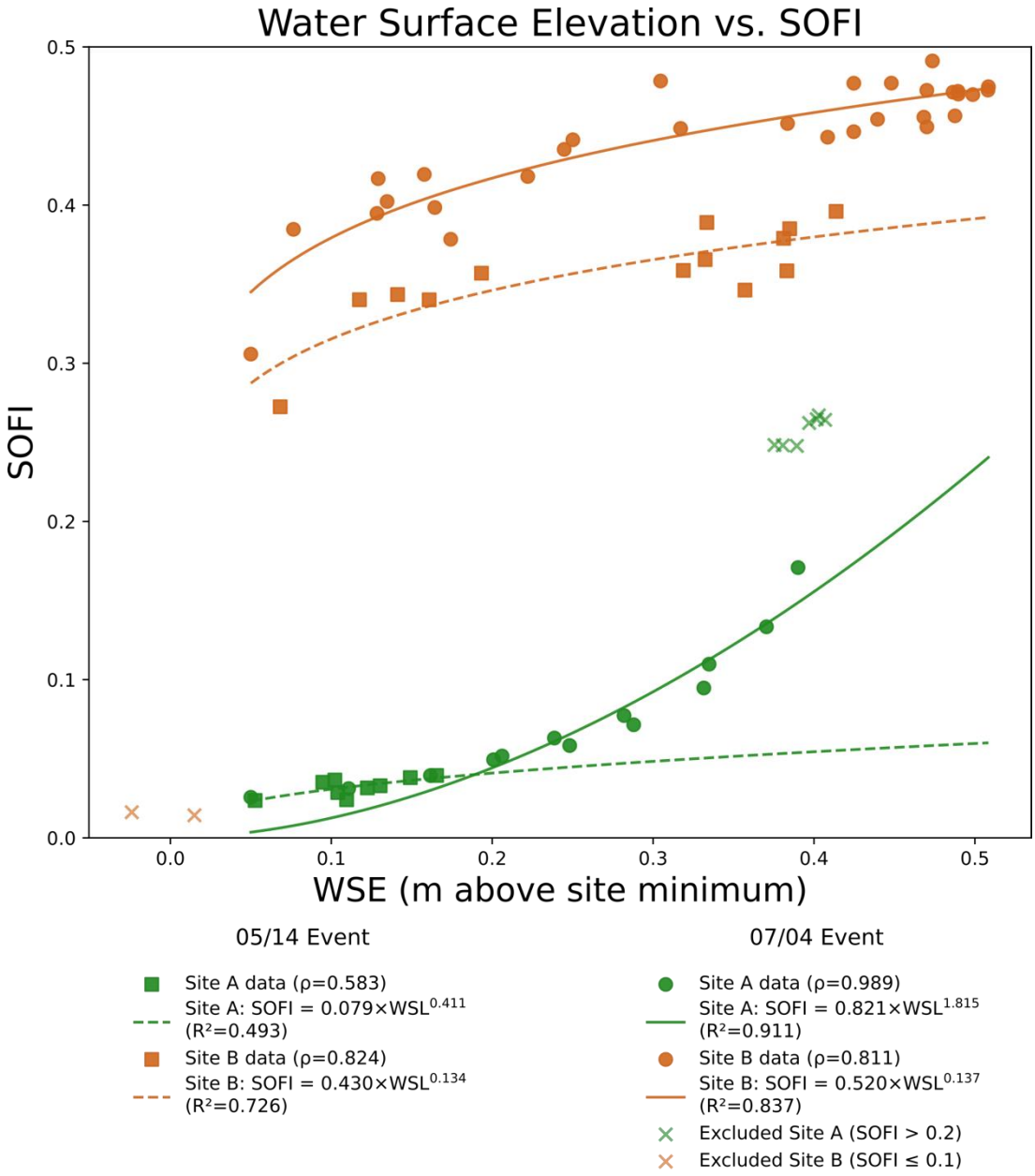

Figure S3: Fitted power law relationships between image derived Water Surface Elevation (WSE_{90}) and Static Observer Flooding Index *(SOFI)*. Water extension towards the camera (decreasing ground pixel size) produces an exponent > 1, such as the July event at Site A (green circles), while water extension away from the camera (increasing ground pixel size), produces an exponent < 1, such as at Site B (orange circles and squares). Images at Site A where flood extent passed the bottom of the image, and images of isolated puddles at Site B were excluded from fitting and are indicated by "X" symbols.

Camera pose estimation error evaluation

	Ground control point estimated			*Static feature estimated*				*IMU*
	ΔC	R_{IMU}	$R_{initial}$	ΔC	R_{IMU}	R_{inital}	R_{GCP}	R_{inital}
Pose 1	0.06 m	2.11°	0.00°	0.07 m	2.14°	0.0°	0.17°	0.00°
Pose 2	0.06 m	1.63°	5.30°	0.10 m	1.65°	5.48°	0.11°	5.18°
Pose 3	0.04 m	1.52°	14.93°	0.17 m	1.62°	15.09°	0.27°	14.78°

Table S3: Camera position (*ΔC*) and rotation errors *(R)* from the camera-lidar calibration test

For the case study events, camera pose was calculated based on available pre-existing static features rather than explicitly surveyed Ground Control Points (GCPs). A calibration test was performed to evaluate pose accuracy when using static features, compared to GCPs. The same model of trail-camera used in the study was mounted to a stable tripod, placed in an outdoor courtyard, and affixed with a 9-axis Inertial Measurement Unit (IMU) to record camera rotation, with a resolution of 0.01 degrees. With the tripod base stationary, images were taken from three different camera orientations. Within practical limits, camera roll and yaw were kept constant, only adjusting camera pitch over a range of 15 degrees. Three lidar scans were collected simultaneously with photo collection. 21 reflective targets were deployed throughout the image field-of-view as ground control points. 22 static features including window corners, fence posts, and utility poles were also identified. Three lidar scans were collected of the scene. Following camera calibration, both GCPs and static features were labeled in the images and point cloud. Three rotation-translation matrices (**P**) were calculated for each camera pose. Our ground truth pose was calculated from IMU measured *X, Y, Z* rotation, and point cloud labeled camera location. The second was estimated from our labeled GCPs using RANSAC optimized EPnP (Lepetit et al., 2009). The third was estimated from our labeled static features in the same manner.

Position error is characterized by the absolute distance between labeled and recovered *X, Y, Z* camera locations (ΔC). Absolute camera rotation error (R_{IMU}) was characterized by the magnitude of rotation between separating the IMU measurements and the estimated rotation matrix. Similarly, relative rotation error ($R_{initial}$) was characterized by the magnitude of rotation from the initial camera position, Pose 1, as calculated by each method. Error in camera location was overall slightly higher when only using static features, but in all cases remained less than 20 cm. Absolute rotation errors were similar between approaches, and all below 2.5°. Rotations relative to the initial camera pose are more consistent, with an average difference of 0.14° and 0.31° from the IMU for GCP and static feature estimates respectively, suggesting a potential offset between the IMUs calibration and the point cloud. This gives us some expectation for the camera pose accuracy achievable with our camera and lidar equipment, in outdoor conditions similar to those of our flood monitoring stations.

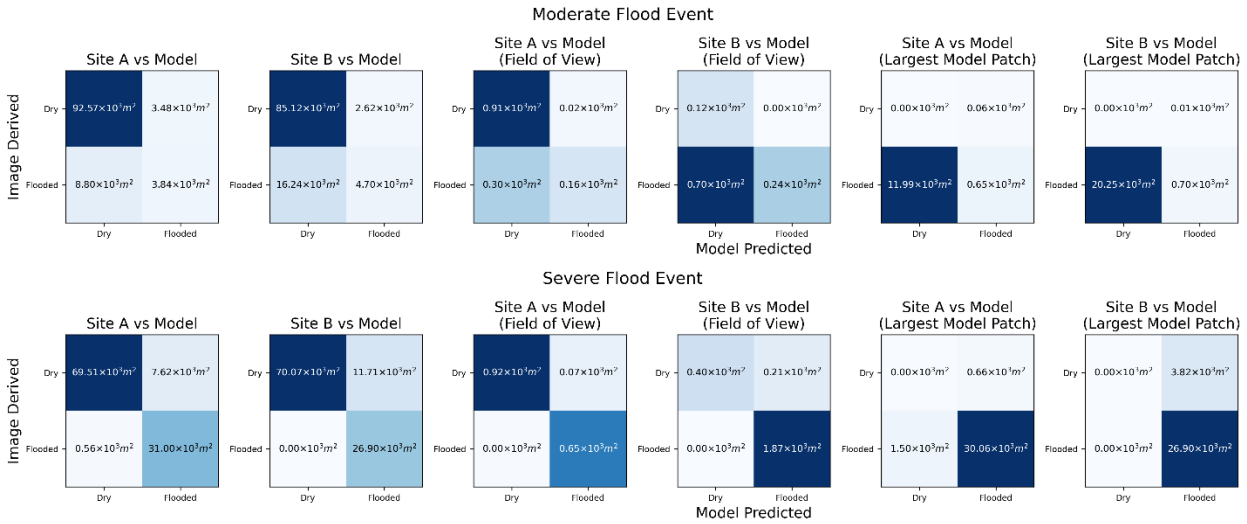

Figure S4: Confusion matrices for image-derived and 2D model predicted peak flood extents. Values indicate the area of overlap and disagreement in flooded and non-flooded raster cells between the methods. Comparisons are shown for the full model extent, restricted to the camera FOV, and restricted to the largest contiguous patch of predicted flooding.

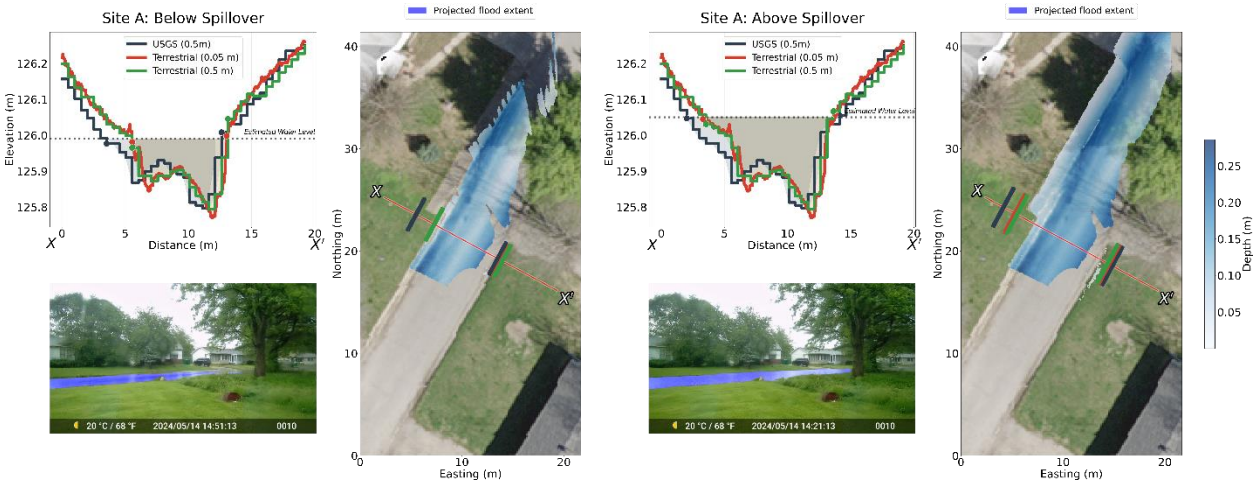

Figure S5: Road topographic profiles based on the 0.5m USGS DTM (black), 0.005m terrestrial DTM (red), and 0.5m terrestrial DTM (green). Flood mask overlays are shown with the corresponding flood extent interpolated from the mask intersection with the projected terrestrial lidar points.

To qualitatively validate the water level extraction method, we examined observation immediately above and below overtopping of the road boundary. These were compared against across-road elevation profiles extracted from both USGS and terrestrial DTMs. Prior to spillover, the projected flood extent ends at the road boundary, with water level slightly below the curb elevation found in the terrestrial DTM profile. After spillover, the project extent expands to fill the small, paved area above the road surface, before stopping at the lawn boundary. This is consistent with the image observation, and topographic profile of a second spillover onto the lawn itself. Further from camera, toward the northwest, decreased pixel resolution leads to the projected extent bleeding beyond the road, potentially upwardly biasing estimated water levels. The extracted water level is approximately 3 cm higher than the elevation

contour best aligned with the projected flood boundary below spillover, and approximately 1 cm higher after spillover. The magnitude of both these biases decreases with larger flood extents due to more gradual elevation gradients, and the lack of curb shadows.

References

HeartLands Conservancy: Prairie Du Pont & Judy's Branch Watershed Plan: Volume One Final Report, Tech. rep., HeartLands Conservancy, https://heartlandsconservancy.org/pdp, last access: 9 Mar 2026, 2023.

Hawkins, R., and Jiang, R.: Runoff curve number method: Examination of the initial abstraction ratio, https://ponce.sdsu.edu/hawkins_initial_abstraction.pdf, last access: 9 Mar 2026.

Illinois State Water Survey. (2018). St. Clair County Building Footprints, Illinois Flood Maps. Retrieved from https://www.illinoisfloodmaps.org/building- footprints.aspx

Multi-Resolution Land Characteristics Consortium: National Land Cover Database (NLCD), USGS ScienceBase Catalog, https://www.sciencebase.gov/catalog/item/6345b637d34e342aee0863aa, 2023.

OpenCV Team: Camera calibration (Python), OpenCV Documentation, https://docs.opencv.org/4.x/dc/dbb/tutorial_py_calibration.html, last access: 9 Mar 2026, 2024.

USACE Floodplain Management Services: Cahokia Heights & East St. Louis Flood Hazard Analysis, Tech. rep., U.S. Army Corps of Engineers, St. Louis, Missouri, https://www.mvs.usace.army.mil/Missions/Programs-Project-Management/Cahokia-Heights, last access: 9 Mar 2026, 2023.

USACE Floodplain Management Services: Piat Place & Harding Ditch Flood Hazard Analysis, Tech. rep., U.S. Army Corps of Engineers, St. Louis, Missouri, https://www.mvs.usace.army.mil/Missions/Programs-Project-Management/Cahokia-Heights, last access: 9 Mar 2026, 2024.

USACE Hydrologic Engineering Center: HEC-RAS Hydraulic Reference Manual: Version 6.6, U.S. Army Corps of Engineers, Davis, California, https://www.hec.usace.army.mil/software/hec-ras/documentation.aspx, last access: 9 Mar 2026, 2024.

USACE Hydrologic Engineering Center: Creating land cover Manning's n values and impervious layers, HEC-RAS 2D User Manual (v6.6), https://www.hec.usace.army.mil/confluence/rasdocs/r2dum/6.6/developing-a-terrain-model-and-geospatial-layers/creating-land-cover-mannings-n-values-and-impervious-layers, last access: 9 Mar 2026.